



1 **Effects of aerosol-radiation interaction on precipitation during**
2 **biomass-burning season in East China**

3

4 **Xin Huang^{1,2,3}, Aijun Ding^{1,2,3*}, Lixia Liu^{1,2}, Qiang Liu^{1,2}, Ke Ding^{1,2}, Wei Nie^{1,2,3}, Zheng**
5 **Xu^{1,2,3}, Xuguang Chi^{1,2,3}, Minghuai Wang^{1,2,3}, Jianning Sun^{1,2,3}, Weidong Guo^{1,2,3}, and**
6 **Congbin Fu^{1,2,3}**

7

8 ¹Joint International Research Laboratory of Atmospheric and Earth System Sciences, Nanjing
9 University, 210023, China

10 ²Institute for Climate and Global Change Research & School of Atmospheric Sciences,
11 Nanjing University, Nanjing, 210023, China

12 ³Collaborative Innovation Center of Climate Change, Jiangsu Province, China

13

14 * Correspondence to: Aijun Ding (dingaj@nju.edu.cn)

15



16 Abstract

17 Biomass burning is a main source for primary carbonaceous particles in the atmosphere and
18 acts as a crucial factor that alters Earth's energy budget and balance. It is also an important
19 factor influencing air quality, regional climate and sustainability in the domain of Pan-
20 Eurasian Experiment (PEEX). During the exceptionally intense agricultural fire season in
21 mid-June 2012, accompanied with rapidly deteriorating air quality, a series of meteorological
22 anomalies was observed, including a large decline in near-surface air temperature, spatial
23 shifts and changes in precipitation in Jiangsu Province of East China. To explore the
24 underlying processes that link air pollution to weather modification, we conducted a
25 numerical study with parallel simulations using the fully coupled meteorology-chemistry
26 model WRF-Chem with a high-resolution emission inventory for agricultural fires. Evaluation
27 of the modelling results with available ground-based measurements and satellite retrievals
28 showed that this model was able to reproduce the magnitude and spatial variations of fire-
29 induced air pollution. During the biomass-burning event in mid-June 2012, intensive emission
30 of absorbing aerosols trapped a considerable part of solar radiation in the atmosphere and
31 reduced incident radiation reaching the surface on a regional scale, followed by lowered
32 surface sensible and latent heat fluxes. The perturbed energy balance and re-allocation gave
33 rise to substantial adjustments in vertical temperature stratification, namely surface cooling
34 and upper-air heating. Furthermore, intimate link between temperature profile and small-scale
35 processes like turbulent mixing and entrainment led to distinct changes in precipitation. On
36 one hand, by stabilizing the atmosphere below and reducing the surface flux, black carbon-
37 laden plumes tended to dissipate daytime cloud and suppress the convective precipitation over
38 Nanjing. On the other hand, heating aloft increased upper-level convective activity and then
39 favored convergence carrying in moist air, thereby enhancing the nocturnal precipitation in
40 the downwind areas of the biomass burning plumes.

41

42 1 Introduction

43 Biomass burning, defined as open or quasi-open combustion of non-fossilized vegetative or
44 organic fuel, is widely used by humans to manage and transform land cover for many
45 purposes and has been identified as one of the most important disturbance agents in world's
46 terrestrial ecosystems (Fearnside, 2000). It is a major source of many trace gases and
47 particulate matters on a regional and a global scale (Andreae and Merlet, 2001; van der Werf



48 et al., 2006; Ito et al., 2007), contributing significantly to the budgets of trace gases,
49 greenhouse gases and atmospheric aerosols (Langenfelds et al., 2002). For instance, biomass
50 burning is estimated to be responsible for almost half of global carbon monoxide (CO)
51 emission and more than one third of total black carbon (BC) emission (Bergamaschi et al.,
52 2000; Bond et al., 2013). With tremendous and intensive emission of atmospheric pollutants,
53 it has been recognized as one of the culprits of regional air pollution (Wiedinmyer et al., 2006;
54 Ryu et al., 2007) and an important disturber of biogeochemical cycles, especially for those of
55 carbon and nitrogen (Crutzen and Andreae, 1990; Kuhlbusch, 1998). In the Eurasian
56 continent, i.e., the domain of Pan-Eurasian Experiment (PEEX) (Kulmala et al., 2015),
57 biomass burning is a very important source influencing air quality, regional climate change
58 and sustainability (Chi et al., 2013; Ding et al., 2013ab; Lappalainen et al., 2016). In the East
59 China, the impact of biomass burning to air quality and regional climate change is particularly
60 interesting because of the mixing of biomass burning plumes with pollutant from fossil fuel
61 combustion sources (Ding et al., 2013a; Nie et al., 2015; Xie et al., 2015; Lappalainen et al.,
62 2016).

63 Biomass burning, including forest fires, savanna fires, peat burning, and crop residue burning
64 in field, generally features a high emission rate of light-absorbing carbonaceous aerosols
65 (Reid et al., 1998; Schwarz et al., 2008). The most important one is BC, which is intensively
66 emitted during biomass burning events due to incomplete combustions (Reid et al., 2005;
67 Akagi et al., 2011). As the dominant absorber of solar radiation in the atmosphere, BC warms
68 the Earth-atmospheric system and alters the partitioning of energy between the ground surface
69 and the atmosphere, thereby modifying atmospheric thermodynamic structures and
70 modulating hydrological cycles (Krishnan and Ramanathan, 2002; Ramanathan et al., 2005;
71 Qian et al., 2014; Saide et al., 2015; Ding et al., 2016). These modifications induced by
72 biomass burning have been detected in many regions, especially for those during forest fires.
73 Surface temperature decline was extensively observed during forest fires in North America,
74 Asia and Africa (Robock, 1988, 1991; Procopio et al., 2004; Kolusu et al., 2015). By cooling
75 the surface and stabilizing the atmosphere, intense forest fire may lead to the inhibition of
76 cloud formation (Andreae et al., 2004; Koren et al., 2004; Feingold et al., 2005), suppression
77 in precipitation (Rosenfeld, 1999; Sakaeda et al., 2011), and even temporal shift in onset of
78 monsoon (Liu et al., 2005; Lau et al., 2006; Zhang et al., 2009). In one word, BC has been
79 demonstrated to cause a significant perturbation in the radiative energy balance and has even



80 led to global climate change (Penner et al., 1992; Menon et al., 2002; Ramanathan and
81 Carmichael, 2008).

82 Although forest and savanna fires are much less notable in China compared with tropical
83 America, Africa and Southeast Asia (van der Werf et al., 2006), it is noteworthy that China is
84 a large agricultural country with the world's top-ranked agricultural production, which is
85 inevitably accompanied by a tremendous amount of crop residue. Field burning of crop
86 residue is a common and wide-spread management practice in China during post-harvest
87 periods for the purpose of clearing farmland and providing short-lived ash fertilization for the
88 crop rotation (Gao et al., 2002). It is estimated that about 120 Tg crop residues were burned in
89 field across China every year, far higher than those burned in forest fires and savanna fires
90 (Yan et al., 2006). Previous studies have documented that field burning of crop residue led to
91 deterioration in regional air quality during harvest season (Yang et al., 2008; Huang et al.,
92 2012b; Li et al., 2014). What is worse, this kind of pollution occurs periodically in East China,
93 particularly during the harvest period of wheat in June (Figure 1). However, studies regarding
94 its effects on meteorology and climate are still limited. Ding et al. (2013a) reported that
95 temperature and precipitation were dramatically modified during the harvest season in 2012
96 according to ground based measurements at a regional background station SORPES in the
97 Yangtze River Delta region in East China (Ding et al., 2013b). However, there is a lack of a
98 comprehensive picture of how or through which processes the biomass burning plumes
99 influenced the air temperature and precipitation and on what scale the aerosol-weather
100 interactions happened during this case.

101 Here we conducted numerical simulations for the biomass burning event in East China during
102 mid-June 2012 based on the online coupled meteorology–chemistry model WRF-Chem (the
103 Weather Research and Forecasting model coupled with Chemistry) combined with multiple
104 ground-based measurements and remote-sensing retrievals. The rest of this paper is structured
105 as follows: Section 2 describes the development of an emission inventory for field burning of
106 crop residues and how the numerical simulations are configured and designed; in Section 3
107 we validate the modelling results using available measurements, and then analyse the
108 perturbations in energy budget and temperature adjustments induced by crop residue burning;
109 finally, three regions with distinct precipitation changes, located near or downwind from the
110 burning sites, are selected to discuss in detail. Conclusions are drawn in Section 4.

111



112 2 Data and Methodology

113 2.1 Emission inventory

114 Modelling aerosols' radiative effects during this biomass burning event first requires accurate
115 quantification and meticulous characterization of emission from field burning of crop residue.
116 Here, emission intensities of trace gases and particulate matters, specifically including carbon
117 dioxide (CO₂), carbon monoxide (CO), methane (CH₄), Non-Methane Organic Compounds
118 (NMOCs), nitrogen oxides (NO_x), ammonia (NH₃), sulfur dioxide (SO₂), black carbon (BC),
119 organic carbon (OC), and particulate matter (PM_{2.5} and PM₁₀ are particles with aerodynamic
120 diameter less than 2.5 and 10 microns, respectively), were estimated based on a bottom-up
121 method. According to the farming season (available at zzys.agri.gov.cn) and province-level
122 statistics on crop cultivation (NBSC, 2013), we can deduce that intensive agricultural fires in
123 June were mainly related to wheat straw burning as a consequence of the extensively
124 spreading cultivation mode of "winter wheat-summer corn" in East China. Burned biomass at
125 province-level was calculated based on statistical data of crop productions, residue-to-
126 production ratios, percentages of crop residues burned in the field. Emissions of various
127 pollutants were derived from the product of burned mass and experiment results on crop-
128 specific combustion efficiencies and pollutant-specific emission factors. The detailed methods
129 and involved datasets are described in our previous work (Huang et al., 2012a). To determine
130 the locations and time of crop residue fires, MODIS (Moderate Resolution Imaging
131 Spectroradiometer) Thermal Anomalies/Fire Daily L3 Global Product (MOD/MYD14A1)
132 combined with burned area product (MCD45A1) were introduced for the purpose of emission
133 spatiotemporal allocations (Giglio et al., 2003; Boschetti et al., 2009). MOD/MYD14A1
134 provides fire identification by examining the brightness temperature relative to neighbouring
135 pixels. MCD45A1 was also incorporated because its bidirectional reflectance model-based
136 change detection approach has been proved to be capable of presenting a more accurate
137 mapping of smaller fragments of burn scars (Roy and Boschetti, 2009). The spatial pattern of
138 fire detections in Figure 2a indicates that open burning of straw mostly concentrated in
139 northern parts of Anhui and Jiangsu province and got extremely severe on 9 and 13 June, as
140 displayed in Figure 2b. Burning of crop residues dominated local emissions of atmospheric
141 pollutants. Taking BC for instance (Figure 2c and d), emission from field burning of crop
142 residue far outweighed that from industry, power plant, residential activity and transportation
143 combined (Li et al., 2015).



144 2.2 Numerical simulation

145 The numerical simulations in this study were conducted using WRF-Chem version 3.6.1,
146 which is an online-coupled chemical transport model considering multiple physical and
147 chemical processes, including emission and deposition of pollutants, advection and diffusion,
148 gaseous and aqueous chemical transformation, aerosol chemistry and dynamics (Grell, G. et
149 al., 2011). The model has been widely utilized to evaluate aerosol-radiation-cloud interactions
150 and aerosol-boundary layer feedback (Grell, G. et al., 2011; Zhao, C. et al., 2013; Fan et al.,
151 2015; Huang et al., 2015; Ding et al., 2016). In the present work, we adopted two nested
152 model domains centred at 115.0 °E, 33.0 °N (Figure 1a). The parent domain with a grid
153 resolution of 20 km covered the eastern China and its surrounding areas to get synoptic
154 forcing. The fine resolution of 4 km for the inner one allowed better characterization of small-
155 scale physical processes, especially those linked to convective motions, cloud formation and
156 rainfall onset. There were 31 vertical layers from the ground level to the top pressure of 50
157 hPa, 20 of which were placed below 4 km. The initial and boundary conditions of
158 meteorological fields were updated from the 6-hour NCEP (National Centres for
159 Environmental Prediction) global final analysis (FNL) data with a 1° × 1° spatial resolution.
160 The simulation was conducted for the time period from 20 May to 15 June, 2012, during
161 which each run covered 60 hours and the last 48-hour modelling results were kept. The
162 chemical outputs from the preceding run were used as the initial conditions for the next run.
163 First two weeks were regarded as the model spin-up period, so as to minimize the influences
164 of initial conditions and allow the model to reach a state of statistical equilibrium under the
165 applied forcing (Berge et al., 2001; Lo et al., 2008).

166 Key parameterization options for the WRF-Chem modelling were the Noah land surface
167 scheme to describe the land-atmosphere interactions (Ek et al., 2003), the YSU boundary
168 layer scheme (Hong, 2010), and the RRTMG short- and long-wave radiation scheme (Mlawer
169 et al., 1997). The Lin microphysics scheme that accounts for 6 forms of hydrometeor (Lin et al.,
170 1983) together with the Grell cumulus parameterization was applied to reproduce the cloud
171 and precipitation processes (Grell, G. A. and Devenyi, 2002) for the coarse domain. Cumulus
172 parameterization was switched off for the inner domain. Previous studies have shown that,
173 under highly polluted conditions, the ARI dominated over the aerosol-cloud interaction (ACI)
174 that is related to aerosols' ability to act as CCN (e.g., Rosenfeld et al., 2008; Fan et al., 2015).
175 Since the focus of this study is on ARI, the prognosed aerosol was disabled to act as cloud



176 condensation nuclei (CCN) or ice nuclei (IN) in our simulations and therefore the effects from
177 ACI were not accounted for. For the numerical representation of atmospheric chemistry, we
178 used the CBMZ (Carbon-Bond Mechanism version Z) photochemical mechanism combined
179 with MOSAIC (Model for Simulating Aerosol Interactions and Chemistry) aerosol model
180 (Zaveri and Peters, 1999; Zaveri et al., 2008). Aerosols were assumed to be spherical particles.
181 The size distribution was divided into four discrete size bins defined by their lower and upper
182 dry particle diameters (0.039–0.156, 0.156–0.625, 0.625–2.5, and 2.5–10.0 μm). Aerosols in
183 each size bin were assumed to be internally mixed and their optical properties, including
184 extinction coefficient, single-scattering albedo (SSA) and asymmetry factor, were computed
185 based on Mie theory (Fast et al., 2006) and volume averaged refractive indices (Barnard et al.,
186 2010). Similar model configurations and settings have achieved good performance in our
187 previous simulations over the eastern China (Huang et al., 2015; Ding et al., 2016). Detailed
188 configurations and domain settings are listed in Table 1.

189 Both natural and anthropogenic emissions were included for the regional WRF-Chem
190 modelling in the present work. Typical anthropogenic emissions were obtained from the
191 Multi-resolution Emission Inventory for China (MEIC) database (Li et al., 2015), in which
192 emissions sources were classified into five main sectors: power plants, residential combustion,
193 industrial processes, on-road mobile sources, and agricultural activities. This database
194 covered most of anthropogenic pollutants, such as SO_2 , NO_x , CO, volatile organic
195 compounds (VOCs), NH_3 , PM, BC, and OC. VOCs emitted from typical anthropogenic
196 activities and aforementioned crop residue burning were speciated into model-ready lumped
197 species using profiles for Carbon-Bond Mechanism (Hsu et al., 2006). The biogenic VOC and
198 NO emissions were calculated online by using the Model of Emissions of Gases and Aerosols
199 from Nature (MEGAN) embedded in WRF-Chem (Guenther et al., 2006). More than 20
200 biogenic species, including isoprene, monoterpenes (e.g., α -pinene and β -pinene) and
201 sesquiterpenes, were considered and then involved in the photochemistry calculation.

202 In order to disentangle aerosols' role in radiative transfer and subsequent effects on cloud and
203 precipitation during this biomass-burning event in the mid-June of 2012, we designed two
204 parallel numerical experiments. Domain settings and model configurations for these two
205 simulations were exactly the same as mentioned before, except that one experiment (aerosol-
206 radiation interaction, ARI) took account of aerosols' perturbations in radiation balance while



207 the other experiment (CTL) did not include any aerosol's effects on either longwave or
208 shortwave radiation.

209 **3 Results and discussions**

210 **3.1 Fire-induced pollution and observed anomalies in meteorology**

211 As demonstrated by existing studies (Andreae et al., 1988; Huang et al., 2012b; Ding et al.,
212 2013a), air quality was dramatically deteriorated and the visibility was impeded during
213 biomass burning events. We compare the simulated PM₁₀ concentration with daily
214 measurements derived from Air Pollution Index (API) in Figure 3 (If not mentioned specially,
215 the simulation refers to ARI experiment hereafter). Both observations and simulations
216 manifested the fact that intensive agricultural fires led to the severe pollution in mid-June.
217 Since 9 June when the detected fire spots became intense and extensive, PM₁₀ concentrations
218 in northern Anhui and northwest Jiangsu province began to increase, especially for those
219 regions near the fire location. For instance, the observed daily mean PM₁₀ concentrations
220 reached up to around 250 µg/m³ at Fuyang (FY) and Xuzhou (XZ) and even exceeded 400
221 µg/m³ at Bengbu (BB) on 9 June (the locations of cities mentioned in this article are labelled
222 in Figure 2). XZ and BB suffered from the second-round fire smoke two days later, with a
223 maximum daily mean concentration of 548 µg/m³ observed at BB. Figure 4 illustrates the
224 satellite-retrieved 660-nm aerosol optical depth (AOD) and SSA from MODIS Aerosol
225 Product MOD04_L2 (daily level 2 data produced at the spatial resolution of 10 km, collection
226 6) around 11:00 local time (LT) on 9 June when the first-round of extensive fire pollution
227 broke out. Their comparisons with modelled spatial distributions of PM_{2.5} and BC column-
228 integrated mass loadings further confirm model's ability to well reproduce atmospheric
229 pollution for this event. The AOD observation shows that high aerosol loadings were
230 concentrating in northeast Anhui and the north-central Jiangsu, shaping a belt of pollution
231 from the fire sites to the downwind areas. The similar pattern was also simulated by the model.
232 The PM_{2.5} mass loading was found to exceed 200 mg/m² near BB, NJ and most parts of
233 central Jiangsu. This strap-shaped pollution was particularly obvious in terms of BC column
234 concentrations, which was also consistent with a relatively lower SSA along BB, Yangzhou
235 (YZ) and Taizhou (TZ).

236 Along with the severe air pollution and poor visibility, anomalies in meteorology occurred on
237 9-10, June. Ding et al. (2013a) found that, during these two days, a sharp decline existed in



238 the observed air temperature in NJ and YZ, compared with weather forecast results and NCEP
239 FNL data, but the simulations and observations showed a good agreement when the heavy air
240 pollution was not present before 8 June. At YZ the temperature difference was as high as 5.9
241 and 9.2 °C on 9 and 10 June, respectively. Simultaneously, measured solar radiation intensity
242 and sensible heat flux showed very low values on 10 June in comparison with non-episode
243 days. Moreover, local meteorological agency forecasted a convective rainfall to occur in NJ
244 and surrounding areas in the afternoon of 10 June, with the rainfall centre passing by NJ
245 around 14:00 LT. However, this forecasted rainfall never happened that day.

246 On the basis of ground-based measurements, vertical sounding data, remote-sensing images
247 and their comparisons with numerical simulations, we found that agricultural fires worsen
248 regional air quality to a large extent and caused a series of anomalies in temperature and
249 precipitation in the mid-June of 2012. How the biomass burning plumes influenced the air
250 temperature and precipitation will be the main issue to be addressed in the following
251 discussions.

252 3.2 Perturbations in energy budget and temperature responses

253 To better understand aerosols' role in the energy balance on 10 June when precipitation was
254 evidently modified, radiative forcing in the atmosphere and at the ground surface was
255 estimated by differentiating the ARI and CTL results (Figure 5). At the surface, daily mean
256 incident short-wave radiation was weakened by 45.5 W/m² (averaged over the inner domain)
257 as the extinction of aerosol was quite large with a satellite-observed 660-nm AOD exceeding
258 2.0 (Figure 4b). Meanwhile, about 60.4 W/m² shortwave energy was blocked in the
259 atmosphere over the inner domain due to the fact that absorbing aerosols were accumulated
260 on that day (Figure 5b). A positive domain-averaged radiative forcing of +14.9 W/m² was
261 simulated at the top of the atmosphere (TOA) on 10 June. Radiation measurements collected
262 at Heifei (HF) and sensible and latent heat flux recorded at Lishui (in South Nanjing) are
263 compared with the diurnal variations of corresponding simulations in Figure 6, which
264 supports that significant radiative perturbations took place at NJ and HF. Substantially
265 weakened daytime solar irradiance was observed on 10 June, when the peak value of
266 downwelling shortwave radiation at HF was 618.3 W/m² at HF and was only 309.7 W/m² at
267 NJ. ARI tended to predict lower downwards solar radiation, which was closer to observation
268 for both cities. Reduction in shortwave energy hitting the surface in turn decreased outgoing



269 heat fluxes, and therefore simulated sensible and latent heat fluxes at 12:00 LT on 10 June in
270 ARI decreased by 89.3 and 76.1 W/m², respectively, compared with CTL experiment.

271 Spatially, the magnitude of the radiative forcing on 10 June was comparable in northern
272 Anhui and central Jiangsu, differing from the distribution pattern of fire-induced air pollution
273 that remarkably concentrated in northern Anhui (Figure 5). As revealed in our previous
274 estimation, among all components of the ambient aerosols, BC is the most important disturber
275 of shortwave radiation transfer at the surface and in the atmosphere as well (Huang et al.,
276 2015; Ding et al., 2016). Although fire emission mostly concentrated in the northern Anhui
277 and resulted in a high BC concentration of 20 µg/m³ there, high-altitude BC was spread much
278 more broadly. At an altitude of 2 km, BC concentration around 5 µg/m³ stretched from
279 northern Anhui to central Jiangsu (Figure 5d). Such distinct distributions between two layers
280 were partly attributed to the stagnant condition near the surface and stronger horizontal
281 transport in the upper level. It is emphasized that upper-level BC has higher absorbing
282 efficiency (Ding et al., 2016). That is why the distributions of both positive radiative forcing
283 in the atmosphere and negative forcing at the surface generally consisted with BC's spatial
284 pattern in the upper air.

285 The perturbations in the energy budget and the following re-allocation gave rise to substantial
286 modulation in temperature stratification. In comparison with CTL experiment, ARI
287 experiment predicted an obvious decline in near-surface temperature by considering the
288 effects of aerosol-radiation interaction. Hourly observed 2-m air temperature was compared
289 with corresponding simulations by two experiments during the time period from 8 to 15 June.
290 Model-performance statistics including mean bias (MB), mean error (ME) and root mean
291 square error (RMSE) are presented in Table 2. As shown, CTL simulation had a systematic
292 positive bias in 2-m temperature and ARI predicted lower temperature for both areas near fire
293 locations (BB and XZ) and downwind regions (NJ and SY). The decreases in temperature
294 were pronounced in BB and XZ with a large difference of approximately 1.2 °C, which
295 notably narrowed the gaps with observations. On 10 June when the fire-induced pollution
296 became intensive, the magnitude of surface cooling was remarkably high near the fire sites
297 (Figure 5e). For instance, compared to CTL, ARI simulated near-surface temperature at XZ
298 was cooled by almost 8.0 °C at 20:00 LT on 10 June (Figure 7b). In addition to the cooling
299 tendency of near-surface temperature, aerosols' radiative effects also increased air
300 temperature at a higher altitude, which were more apparent over the downwind areas (Figure



301 5f). According to the comparisons between simulated temperature profiles by the two parallel
302 experiments in Figure 7, the warming of air temperature was particularly evident around an
303 altitude of 2 km at SY with a maximum of 3.0 °C.

304 The different temperature responses over the source region of fire emission and downwind
305 areas could be partially interpreted by the fact that near the fire locations pronounced surface
306 cooling counteracted some of atmospheric warming, which would otherwise elevate upper-air
307 temperature, through vertical mixing; while for the downwind area where the surface was less
308 radiatively cooled, the atmosphere was prone to being warmed. As a result of surface cooling
309 and atmospheric heating, vertical convective motions were weakened, triggering perturbations
310 in pressure and wind fields (Figure 5e and f). It is obvious that suppressed convection was
311 generally along with the resultant wind convergence around 2 km and surface divergence,
312 which may further play a significant role in water vapor transport and then cloud formation.

313 **3.3 Effects on cloud and precipitation**

314 In addition to the attenuation of solar radiation and the modulation in temperature gradients,
315 precipitation also showed many disparities between CTL and ARI simulations. The satellite
316 observation from Tropical Rainfall Measuring Mission (TRMM) Multisatellite Precipitation
317 Analysis product (3B42), which provides merged-infrared precipitation information at a
318 $0.25 \times 0.25^\circ$ spatial resolution and has been demonstrated to perform well in East China
319 (Simpson et al., 1988; Zhao and Yatagai, 2014), was used to evaluate the simulated
320 precipitation. As demonstrated in Figure 8, ARI experiment agrees better with TRMM
321 observations in terms of precipitation intensities and also spatial pattern on 10 June.
322 Specifically, CTL simulation suggested a convective rain in Zone 1 (NJ and its adjacent areas)
323 around 14:00 LT (the locations of Zone 1-3 are marked in Figure 8c), however the ARI
324 simulation didn't show any precipitation then, consistent with the TRMM observations.
325 Besides, ARI displayed enhanced precipitation in northern Jiangsu province. A precipitation
326 with the intensity of 3 and 5 mm/h was predicted by ARI in Zone 2 (XZ and its adjacent areas)
327 and Zone 3 (SY and its adjacent areas), which, however, never occurred in CTL experiment.
328 Concerning temporal variations, 3-hour precipitation rates for these three zones derived from
329 TRMM 3B42 retrievals are plotted in Figure 9. Compared to CTL, ARI experiment succeeded
330 in capturing the approximate onset time for all the three regions.



331 The backward trajectories in Figure 2a, which were calculated by HYSPLIT (Hybrid Single
332 Particle Lagrangian Integrated Trajectory Model, Draxler and Rolph, 2003), clearly indicate
333 that the air masses had passed through fire-dense regions before approaching NJ, XZ and SY.
334 Then cloud evaporation in Zone 1 was predicted by ARI, and meanwhile Zone 2 and 3
335 experienced increased nocturnal rainfall on 10 June in ARI experiment. In other words, the
336 spatiotemporal shifts in precipitation during this biomass burning event were closely
337 connected with aerosols' radiative effects.

338 3.3.1 Suppressed daytime precipitation

339 Over Zone 1, CTL produced a convective rainfall event in the afternoon that actually did not
340 happen, while ARI simulation with no precipitation was closer to the observations. From
341 energy budget and radiation flux calculation (Figure 5), on 10 June more than 6 MJ/m^2 solar
342 radiation that supposed to reach the surface was blocked in the atmosphere over Zone 1. The
343 presence of light-absorbing aerosols reduced sensible heat flux and evapotranspiration at the
344 surface (Figure 6). Large-eddy simulation for biomass burning regions of Brazil deduced that
345 the peak reductions in sensible and latent heat flux were 60 and 70 W/m^2 (Feingold et al.,
346 2005), which are quantitatively similar to those near NJ estimated in this work. It was shown
347 that reduced surface flux alone was sufficient to explain the observed cloud dissipation during
348 the biomass burning event in Brazil. For this case, this convective rain got disappeared merely
349 by nudging 2-m temperature in the WRF modelling run by Ding et al. (2013a), highlighting
350 the importance of surface flux modification in the development of these convective clouds.

351 To figure out the role of vertical thermal behaviors in Zone 1, temporal variations of zone-
352 averaged differences in temperature, relative humidity (RH) profiles between ARI and CTL
353 runs are illustrated in Figure 10a and b. From 9:00 LT in the morning, a 1-km-thick belt with
354 BC-laden smoke approached Zone 1 and covered over the boundary layer top. The radiative
355 extinction by the elevated smoke layer led to a cooling effect at the surface, which reduced the
356 boundary layer height and decreased the air temperature in the boundary layer.
357 Simultaneously, relatively strong warming effect between the altitudes of 1-3 km increased
358 the air temperature above the boundary layer. The cooling at the lower altitude and warming
359 at the upper altitude made the stability significantly increased, especially near the top of the
360 boundary layer, which further suppressed the development of boundary layer. For the
361 humidity perturbations, the enhanced stability reduced the boundary layer height and hindered
362 the upward transport of water vapor to a higher altitude, while the heating aloft decreased RH



363 by increasing the air temperature there. These led to a resultant decrease of more than 20% in
364 RH above the boundary layer. A more stable and shallower boundary layer in ARI tended to
365 reduce convective mixing and effectively cut off the cloud layer from its source of moisture,
366 subsequently desiccating the cloud layer, and leading to substantially weakened vertical
367 motions. Accordingly, ARI-simulated updraft velocity above 1 km was only one-tenth that of
368 CTL experiment in the afternoon of 10 June, as demonstrated in Figure 10f. Therefore,
369 compared with CTL, less water vapor condensed above 1 km but accumulated beneath due to
370 much weaker convection in ARI experiment (Figure 10e).

371 In addition to Zone 1, this warmed belt was also blanketing a wider range from 116 to 120 °E
372 at the moment when the CTL-predicted rainfall started (Figure 9a shows that the rainfall
373 occurred around 14:00 LT), as shown in the longitude-height cross sections of temperature
374 difference between CTL and ARI experiment in Figure 10c. In CTL run, cumulus cloud layer
375 appeared above the inversion capping the boundary layer (Figure 10d). However, the
376 absorbing aerosol in ARI run heated the atmosphere aloft and stabilized the sub-cloud layer.
377 The decrease in specific humidity was collocated with warmed upper air since that
378 atmospheric heating and surface cooling weakened vertical convection and further reduced
379 the vertical transport of water vapor. Lower entrainment rate together with higher saturation
380 pressure resulted in daytime decoupling and thinning of the cloud layer all along the longitude
381 from 116 to 120 °E. This effect might be further strengthened by a positive feedback loop as
382 described by Jacobson (2002) in which cloud loss leads to an increasing opportunity for BC's
383 light absorption.

384 3.3.2 Enhanced nocturnal precipitation

385 A precipitation rate of over 2.5 mm/h was observed around 19:00-20:00 LT on 10 June in XZ
386 and its surrounding areas (Zone 2). Only ARI simulation captured this precipitation event. As
387 shown in Figure 11a, there existed two layers with a high BC concentration of up to $10 \mu\text{g}/\text{m}^3$
388 during daytime over Zone 2. One was near the surface and peaked around 18:00 LT, which
389 could be linked to local fire emissions. The other one was lying over the boundary layer top,
390 which was apparent at an altitude of 0.8 km before the boundary layer developed and at 2 km
391 after 15:00 LT. It was very likely to be associated with the transport of upstream fire pollution.
392 Owing to strong radiative heating effect of BC, a warmer layer was formed above 1 km
393 during daytime with temperature increase over 1.0 °C. On the contrary, near-surface
394 temperature kept decreasing. The decline reached its maximum around 20:00 LT. It was also



395 supported by Figure 7b in which the near-surface temperature decreased by almost 8.0 °C at
396 XZ. Until 16:00 LT, the upper-air warming due to radiative absorption was gradually
397 compensated by cooling from the surface through vertical mixing. Changes in RH were
398 almost opposite of those in air temperature. Around 18:00 LT, RH at 3-km altitude started to
399 increase and then a precipitating cloud formed there.

400 To get a better insight on the dynamical processes that contribute to precipitation change,
401 longitude-height cross section of zonal mean responses of temperature, water vapor and wind
402 profile just before the onset time of precipitation are demonstrated in Figure 11c and d.
403 Noteworthy is that warmed upper air between 117 to 119 °E led to less condensation there.
404 More water vapor accumulated below 1 km and was then transported toward Zone 2 by the
405 prevailing east wind near the surface, leading to an excess water vapor over Zone 2 in ARI
406 (Figure 11e). Simultaneously, radiatively heated air parcel with a temperature increase of 0.5
407 °C was found around 2 km over Zone 2. The warmer layer around 2-3 km combined with
408 large drops in temperature beneath resulted in a buoyancy-driven lifting force. Moreover,
409 horizontal heterogeneity in atmospheric heating provided the low-level convergence for
410 maintaining convection in a conditionally unstable atmosphere around 3 km. Thus the zone-
411 averaged updraft velocity in ARI tripled that predicted by CTL at the altitude of 3 km when
412 the precipitation began (Figure 11f). Understandably, what made the precipitating cloud
413 formed around 3 km over Zone 2 were the accumulated moisture near the surface and
414 anomalous updraft of the air that favored the vertical uplift of water vapor. The release of
415 latent heat may increase the upper-air instability and further enhance the precipitation.

416 For the downwind region Zone 3, the warming effect caused by aerosol-radiation interaction
417 was evident for the air column above 0.5 km all day long on 10 June (Figure 12a). The
418 warming pattern was coincident with the distribution of BC concentration since BC is the
419 predominant light-absorbing aerosol specie in the atmosphere. As a result of increased air
420 temperature, RH decreased substantially during daytime. At late night, an extra precipitating
421 cloud formed above 2 km over Zone 3 in ARI simulation, leading to a nocturnal precipitation
422 with a strength of approximately 6 mm/h at 01:00 LT on 11 June. What triggered this rainfall
423 event is a bit complicated than that over Zone 2. First, the whole air column was getting
424 cooled at the moment when the precipitation took place, inevitably raising RH value. The RH
425 increase was quite apparent at the altitude of 3-4 km. Second, daytime radiative absorption by
426 BC-laden plumes around 2 km heated the surrounding air. Relatively warmer layer at the



427 altitude of ~ 2 km generated a positive buoyant updraft (Figure 12f), hence air parcel there
428 was displaced upwards along with enhanced convergence carrying in moist air. This effect
429 has been proposed by Fan et al. (2015) as part of termed “enhanced conditional instability”,
430 by which absorbing aerosols escalate convection downwind of a heavily polluted area and
431 promote precipitation. Last but not the least, spatially heterogeneous aerosol-related heating
432 was associated with greater horizontal temperature lapse, resulting in a convergence flow
433 above 3 km with an additional onshore wind (Figure 12d). Zone 3 is only about 20 km from
434 the Yellow sea. It is plausible that more water vapor-saturated air masses originating from the
435 ocean brought in excess water vapor and consequently elevated the humidity above 3 km
436 (Figure 12e). We suggest that these precipitating clouds formed because of instability at the
437 top of the smoke layer, driven by the strong radiation absorption that warmed the surrounding
438 air. Therefore, the heated BC-laden air was ascended and cooled, leading to the formation of
439 clouds preferentially in the conditionally unstable zone in the upper air.

440 **3.4 Uncertainties**

441 Though the modelling work here characterized cloud and precipitation anomalies during the
442 biomass burning event, we may also question to what extent the modelling reproduced the
443 relevant processes in the real world. As widely acknowledged, accurate simulation of smoke
444 plume and prediction of clouds are both challenging for regional/global models. One
445 contributor to the uncertainties is the characterization of fire emission. The magnitude was
446 determined by statistical information and laboratory experiment data, whose accuracy and
447 representativeness may introduce some uncertainties. The spatiotemporal distribution of fire
448 emission was allocated based on MODIS retrievals. Loss of information due to cloud
449 coverage and poor detection efficiency of short-lived or small-scale fires are major limitations
450 (Giglio et al., 2003). Another challenge is quantification of heat release from biomass burning
451 and subsequent effects on local and regional meteorology. Furthermore, much emphasis has
452 been paid to the vertical distribution of absorbing aerosol, to which the cloud response is
453 highly sensitive (Koch and Del Genio, 2010). The vertical profile of absorbing aerosol in this
454 simulation underwent little constrain due to limited observation at that time. The regional
455 model is hardly capable of precisely presenting turbulent flows and vertical transport, thus
456 introducing uncertainties in three dimensional distributions of BC. It also should be noted that
457 BC is co-emitted with other components such as OC and sulfur dioxide that oxidizes to
458 sulfate (Xie et al., 2015). Mixing with other scattering aerosol would considerably amplify the



459 absorbing efficiency of BC. Model's ability to account for the evolution of mixing state and
460 how to quantify its amplification also affect the simulated radiative behaviors. Besides, poorly
461 recognized secondary organic carbon (SOC) formation processes and its light absorption
462 makes it imperative to reassess and redefine the chemical mechanism and optical properties of
463 OC in models (Saleh et al., 2014). The large uncertainty in simulating clouds and further
464 aerosol-cloud interaction is another limitation (e.g., Wang et al., 2011; Tao et al., 2012). To
465 improve the model performance in all these chemical and physical processes, more
466 comprehensive measurements and modelling efforts are needed in the future.

467

468 **4 Conclusions**

469 To investigate radiative effects of aerosol-radiation interaction on cloud and precipitation
470 modifications during the exceptionally active agricultural fire season in June 2012, a bottom-
471 up emission inventory of crop open burning was developed and then the fully coupled online
472 WRF-Chem model was applied in this work. The evaluation of simulation through ground-
473 based observations and satellite retrievals showed that the model generally captured spatial
474 patterns and temporal variations of fire pollution, which was predominantly concentrating
475 over northern Anhui and central-north Jiangsu. It is evident that post-harvest burning of crop
476 residues emitted a tremendous amount of atmospheric pollutants and deteriorated regional air
477 quality in East China. Elevated concentration of aerosols, particularly light-absorbing BC,
478 would heat the atmosphere and cool the ground surface through both direct solar radiation
479 attenuation (direct radiative forcing) and cloud redistribution (semi-direct radiative forcing).
480 This radiative cooling (heating) effects were distinct close to (downwind from) the source
481 regions of fire sites. Adjusted temperature structure was intimately linked to small-scale
482 processes such as turbulent mixing, entrainment and the evolution of the boundary layer.
483 Subsequently, over NJ and its adjacent regions, absorbing aerosols immediately above the
484 boundary layer top increased the inversion beneath, reducing available moisture and leading
485 to a burn-off effect of cloud. Meanwhile, fire plumes played an enhancement role in nocturnal
486 precipitation over northern Jiangsu by increasing up-level convective activity and fostering
487 low-level convergence that carries in more moist air. Overall, aerosols' radiative effect on
488 precipitation modification is therefore likely to depend to a large extent on local
489 meteorological conditions like atmospheric instability and humidity.

490



491 **Acknowledgements**

492 This work was supported by the National Natural Science Foundation of China
493 (D0512/41422504, D0512/91544231, and D0510/41505109). Part of this work was supported
494 by the Jiangsu Provincial Science Fund for Distinguished Young Scholars awarded to A. J.
495 Ding (No. BK20140021).

496

497



498 Table 1. WRF-Chem modelling configuration options and settings.

Domain setting		
	Domain 1	Domain 2
Horizontal grid	130×130	160×160
Grid spacing	20 km	4 km
Vertical layers	31	31
Configuration options		
Long-wave radiation	RRTMG	
Short-wave radiation	RRTMG	
Land-surface	Noah	
Boundary layer	YSU	
Microphysics	Lin et al.	
Cumulus parameterization	Grell–Deveny (only for domain 1)	
Photolysis	Fast-J	
Gas-phase chemistry	CBMZ	
Aerosol scheme	MOSAIC	

499

500



501 Table 2. Statistical analyses of the simulated 2-m temperature and the corresponding
502 observations at four different cities.

	MB ^a		ME ^a		RMSE ^a	
	CTL	ARI	CTL	ARI	CTL	ARI
NJ	0.85	0.37	1.70	1.66	2.39	2.15
BB	2.19	0.98	2.51	1.65	3.27	2.16
XZ	1.67	0.51	2.37	2.19	3.32	2.89
SY	-0.28	-0.46	1.97	1.65	2.52	2.03

503 ^aMB, ME and RMSE refer to mean bias, mean error and root-mean-square error respectively.

504

505 **References**

- 506 Akagi, S. K., Yokelson, R. J., Wiedinmyer, C., Alvarado, M. J., Reid, J. S., Karl, T., Crouse,
507 J. D., and Wennberg, P. O.: Emission factors for open and domestic biomass burning for use
508 in atmospheric models, *Atmos. Chem. Phys.*, 11, 4039-4072, 10.5194/acp-11-4039-2011,
509 2011.
- 510 Andreae, M. O., Browell, E. V., Garstang, M., Gregory, G. L., Harriss, R. C., Hill, G. F.,
511 Jacob, D. J., Pereira, M. C., Sachse, G. W., Setzer, A. W., Dias, P. L. S., Talbot, R. W., Torres,
512 A. L., and Wofsy, S. C.: Biomass-Burning Emissions and Associated Haze Layers over
513 Amazonia, *J. Geophys. Res. Atmos.*, 93, 1509-1527, doi:10.1029/Jd093id02p01509, 1988.
- 514 Andreae, M. O., and Merlet, P.: Emission of trace gases and aerosols from biomass burning,
515 *Global Biogeochem. Cy.*, 15, 955-966, doi:10.1029/2000gb001382, 2001.
- 516 Andreae, M. O., Rosenfeld, D., Artaxo, P., Costa, A. A., Frank, G. P., Longo, K. M., and
517 Silva-Dias, M. A. F.: Smoking rain clouds over the Amazon, *Science*, 303, 1337-1342,
518 doi:10.1126/science.1092779, 2004.
- 519 Barnard, J. C., Fast, J. D., Paredes-Miranda, G., Arnott, W. P., and Laskin, A.: Technical Note:
520 Evaluation of the WRF-Chem "Aerosol Chemical to Aerosol Optical Properties" Module
521 using data from the MILAGRO campaign, *Atmos. Chem. Phys.*, 10, 7325-7340, 10.5194/acp-
522 10-7325-2010, 2010.
- 523 Bergamaschi, P., Hein, R., Heimann, M., and Crutzen, P. J.: Inverse modeling of the global
524 CO cycle 1. Inversion of CO mixing ratios, *J. Geophys. Res. Atmos.*, 105, 1909-1927,
525 doi:10.1029/1999jd900818, 2000.
- 526 Berge, E., Huang, H. C., Chang, J., and Liu, T. H.: A study of the importance of initial
527 conditions for photochemical oxidant modeling, *J. Geophys. Res. Atmos.*, 106, 1347-1363,
528 doi:10.1029/2000jd900227, 2001.
- 529 Bond, T. C., Doherty, S. J., Fahey, D. W., Forster, P. M., Berntsen, T., DeAngelo, B. J.,
530 Flanner, M. G., Ghan, S., Karcher, B., Koch, D., Kinne, S., Kondo, Y., Quinn, P. K., Sarofim,
531 M. C., Schultz, M. G., Schulz, M., Venkataraman, C., Zhang, H., Zhang, S., Bellouin, N.,
532 Guttikunda, S. K., Hopke, P. K., Jacobson, M. Z., Kaiser, J. W., Klimont, Z., Lohmann, U.,
533 Schwarz, J. P., Shindell, D., Storelvmo, T., Warren, S. G., and Zender, C. S.: Bounding the
534 role of black carbon in the climate system: A scientific assessment, *J. Geophys. Res. Atmos.*,
535 118, 5380-5552, 10.1002/jgrd.50171, 2013.
- 536 Boschetti, L., Roy, D., and Hoffmann, A.: MODIS Collection 5 Burned Area Product-
537 MCD45, User's Guide, Ver, 2, 2009.
- 538 Chi, X., Winderlich, J., Mayer, J.-C., Panov, A. V., Heimann, M., Birmili, W., Heintzenberg,
539 J., Cheng, Y., and Andreae, M. O.: Long-term measurements of aerosol and carbon monoxide
540 at the ZOTTO tall tower to characterize polluted and pristine air in the Siberian taiga, *Atmos.*
541 *Chem. Phys.*, 13, 12271-12298, doi:10.5194/acp-13-12271-2013, 2013.
- 542 Crutzen, P. J., and Andreae, M. O.: Biomass Burning in the Tropics - Impact on Atmospheric
543 Chemistry and Biogeochemical Cycles, *Science*, 250, 1669-1678, doi:10.1126/science.250.
544 4988.1669, 1990.
- 545 Ding, A. J., Fu, C. B., Yang, X. Q., Sun, J. N., Petaja, T., Kerminen, V. M., Wang, T., Xie, Y.,
546 Herrmann, E., Zheng, L. F., Nie, W., Liu, Q., Wei, X. L., and Kulmala, M.: Intense
547 atmospheric pollution modifies weather: a case of mixed biomass burning with fossil fuel



- 548 combustion pollution in eastern China, *Atmos. Chem. Phys.*, 13, 10545-10554, 10.5194/acp-
549 13-10545-2013, 2013a.
- 550 Ding, A. J., Fu, C. B., Yang, X. Q., Sun, J. N., Zheng, L. F., Xie, Y. N., Herrmann, E., Nie,
551 W., Petaja, T., Kerminen, V. M., and Kulmala, M.: Ozone and fine particle in the western
552 Yangtze River Delta: an overview of 1 yr data at the SORPES station, *Atmos. Chem. Phys.*,
553 13, 5813-5830, 10.5194/acp-13-5813-2013, 2013b.
- 554 Ding, A. J., Huang, X., Nie, W., Sun, J. N., Kerminen, V. M., Petäjä T., Su, H., Cheng, Y. F.,
555 Yang, X. Q., Wang, M. H., Chi, X. G., Wang, J. P., Virkkula, A., Guo, W. D., Yuan, J., Wang,
556 S. Y., Zhang, R. J., Wu, Y. F., Song, Y., Zhu, T., Zilitinkevich, S., Kulmala, M., and Fu, C. B.:
557 Black carbon enhances haze pollution in megacities in China, *Geophys. Res. Lett.*,
558 doi:10.1002/2016GL067745, 2016.
- 559 Draxler, R. R., and Rolph, G.: HYSPLIT (HYbrid Single-Particle Lagrangian Integrated
560 Trajectory) model access via NOAA ARL READY website (<http://www.arl.noaa.gov/ready/hysplit4.html>). NOAA Air Resources Laboratory, Silver Spring, in, Md, 2003.
- 562 Ek, M. B., Mitchell, K. E., Lin, Y., Rogers, E., Grunmann, P., Koren, V., Gayno, G., and
563 Tarpley, J. D.: Implementation of Noah land surface model advances in the National Centers
564 for Environmental Prediction operational mesoscale Eta model, *J. Geophys. Res. Atmos.*, 108,
565 Artn 8851, doi:10.1029/2002jd003296, 2003.
- 566 Fan, J. W., Rosenfeld, D., Yang, Y., Zhao, C., Leung, L. R., and Li, Z. Q.: Substantial
567 contribution of anthropogenic air pollution to catastrophic floods in Southwest China,
568 *Geophys. Res. Lett.*, 42, 6066-6075, 10.1002/2015GL064479, 2015.
- 569 Fast, J. D., Gustafson, W. I., Easter, R. C., Zaveri, R. A., Barnard, J. C., Chapman, E. G.,
570 Grell, G. A., and Peckham, S. E.: Evolution of ozone, particulates, and aerosol direct radiative
571 forcing in the vicinity of Houston using a fully coupled meteorology-chemistry-aerosol model,
572 *J. Geophys. Res. Atmos.*, 111, Artn D21305, doi:10.1029/2005jd006721, 2006.
- 573 Fearnside, P. M.: Global warming and tropical land-use change: greenhouse gas emissions
574 from biomass burning, decomposition and soils in forest conversion, shifting cultivation and
575 secondary vegetation, *Climatic change*, 46, 115-158, 2000.
- 576 Feingold, G., Jiang, H. L., and Harrington, J. Y.: On smoke suppression of clouds in
577 Amazonia, *Geophys. Res. Lett.*, 32, Artn L02804, doi:10.1029/2004gl021369, 2005.
- 578 Gao, X., Ma, W., Ma, C., Zhang, F., and Wang, Y.: Analysis on the current status of
579 utilization of crop straw in China (in Chinese), *Journal of Huazhong Agricultural University*,
580 21, 242-247, 2002.
- 581 Giglio, L., Descloitres, J., Justice, C. O., and Kaufman, Y. J.: An enhanced contextual fire
582 detection algorithm for MODIS, *Remote. Sens. Environ.*, 87, 273-282, 10.1016/S0034-
583 4257(03)00184-6, 2003.
- 584 Grell, G., Freitas, S. R., Stuefer, M., and Fast, J.: Inclusion of biomass burning in WRF-Chem:
585 impact of wildfires on weather forecasts, *Atmos. Chem. Phys.*, 11, 5289-5303, 10.5194/acp-
586 11-5289-2011, 2011.
- 587 Grell, G. A., and Devenyi, D.: A generalized approach to parameterizing convection
588 combining ensemble and data assimilation techniques, *Geophys. Res. Lett.*, 29, Artn 1693,
589 doi: 10.1029/2002gl015311, 2002.



- 590 Guenther, A., Karl, T., Harley, P., Wiedinmyer, C., Palmer, P. I., and Geron, C.: Estimates of
591 global terrestrial isoprene emissions using MEGAN (Model of Emissions of Gases and
592 Aerosols from Nature), *Atmos. Chem. Phys.*, 6, 3181-3210, 2006.
- 593 Hong, S. Y.: A new stable boundary-layer mixing scheme and its impact on the simulated
594 East Asian summer monsoon, *Q. J. Roy. Meteor. Soc.*, 136, 1481-1496, doi:10.1002/Qj.665,
595 2010.
- 596 Hsu, Y., Strait, R., Roe, S., and Holoman, D. S.: 4.0. Speciation Database Development
597 Documentation. Final Report. EPA contract. Nos, EP-D-06.001, work assignment Numbers 0-
598 03 and 68-D-02-063, WA 4-04 and WA 5-05. EPA/600/R-06/16. http://www.epa.gov/ttn/chief/software/speciate/speciate4/documentation/speciatedoc_1206.pdf, 2006.
- 600 Huang, X., Li, M. M., Li, J. F., and Song, Y.: A high-resolution emission inventory of crop
601 burning in fields in China based on MODIS Thermal Anomalies/Fire products, *Atmos.*
602 *Environ.*, 50, 9-15, 10.1016/j.atmosenv.2012.01.017, 2012a.
- 603 Huang, X., Song, Y., Li, M. M., Li, J. F., and Zhu, T.: Harvest season, high polluted season in
604 East China, *Environ. Res. Lett.*, 7, Artn 044033, doi:10.1088/1748-9326/7/4/044033, 2012b.
- 605 Huang, X., Song, Y., Zhao, C., Cai, X. H., Zhang, H. S., and Zhu, T.: Direct Radiative Effect
606 by Multicomponent Aerosol over China, *J. Climate*, 28, 3472-3495, 10.1175/Jcli-D-14-
607 00365.1, 2015.
- 608 Ito, A., Ito, A., and Akimoto, H.: Seasonal and interannual variations in CO and BC emissions
609 from open biomass burning in Southern Africa during 1998-2005, *Global Biogeochem. Cy.*,
610 21, Artn Gb2011, doi:10.1029/2006gb002848, 2007.
- 611 Jacobson, M. Z.: Control of fossil-fuel particulate black carbon and organic matter, possibly
612 the most effective method of slowing global warming, *J. Geophys. Res. Atmos.*, 107, Artn
613 4410, doi:10.1029/2001jd001376, 2002.
- 614 Koch, D., and Del Genio, A. D.: Black carbon semi-direct effects on cloud cover: review and
615 synthesis, *Atmos. Chem. Phys.*, 10, 7685-7696, 10.5194/acp-10-7685-2010, 2010.
- 616 Kolusu, S. R., Marsham, J. H., Mulcahy, J., Johnson, B., Dunning, C., Bush, M., and
617 Spracklen, D. V.: Impacts of Amazonia biomass burning aerosols assessed from short-range
618 weather forecasts, *Atmos. Chem. Phys.*, 15, 12251-12266, 10.5194/acp-15-12251-2015, 2015.
- 619 Koren, I., Kaufman, Y. J., Remer, L. A., and Martins, J. V.: Measurement of the effect of
620 Amazon smoke on inhibition of cloud formation, *Science*, 303, 1342-1345, doi: 10.1126
621 /science.1089424, 2004.
- 622 Krishnan, R., and Ramanathan, V.: Evidence of surface cooling from absorbing aerosols,
623 *Geophys. Res. Lett.*, 29, Artn 1340, doi:10.1029/2002gl014687, 2002.
- 624 Kuhlbusch, T. A. J.: Black carbon and the carbon cycle, *Science*, 280, 1903-1904,
625 doi:10.1126/science.280.5371.1903, 1998.
- 626 Kulmala, M., Lappalainen, H.K., Pet ä ä T., Kurten, T., Kerminen, V-M., Viisanen, Y., Hari,
627 P., Bondur, V., Kasimov, N., Kotlyakov, V., Matvienko, G., Baklanov, A., Guo, H., Ding, A.,
628 Hansson, H-C., and Zilitinkevich, S., 2015. Introduction: The Pan-Eurasian Experiment
629 (PEEX) – multi-disciplinary, multi-scale and multi-component researchn and capacity
630 building initiative, *Atmos. Chem. Phys.*, 15, 13085-13096, doi:10.5194/acp-15-13085-2015,
631 2015.



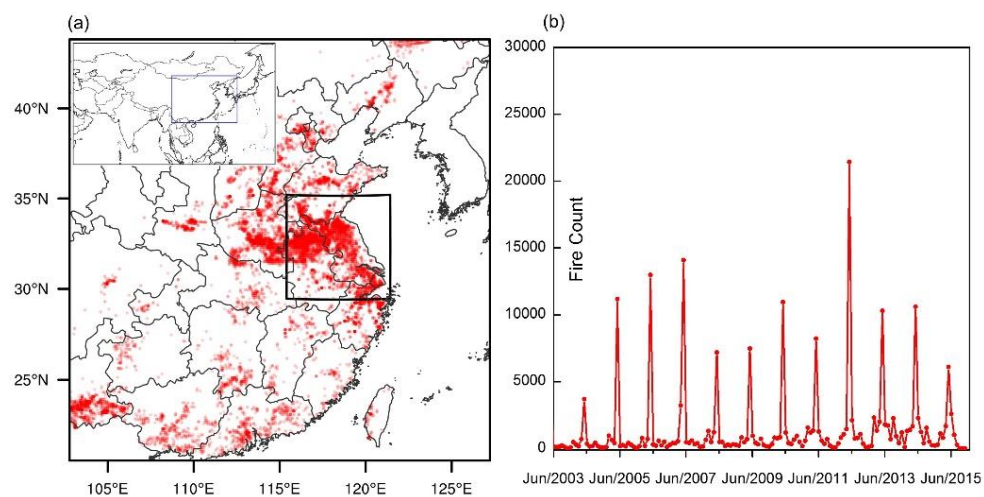
- 632 Langenfelds, R. L., Francey, R. J., Pak, B. C., Steele, L. P., Lloyd, J., Trudinger, C. M., and
633 Allison, C. E.: Interannual growth rate variations of atmospheric CO₂ and its delta C-13, H-2,
634 CH₄, and CO between 1992 and 1999 linked to biomass burning, *Global Biogeochem. Cy.*, 16,
635 Artn 1048, doi:10.1029/2001gb001466, 2002.
- 636 Lappalainen, H.K. et al., Pan-Eurasian Experiment (PEEX): Towards holistic understanding
637 of the feedbacks and interactions in the land-atmosphere-ocean-society continuum in the
638 Northern Eurasian region, submitted to *Atmos. Chem. Phys.*, 2016.
- 639 Lau, K. M., Kim, M. K., and Kim, K. M.: Asian summer monsoon anomalies induced by
640 aerosol direct forcing: the role of the Tibetan Plateau, *Clim. Dynam.*, 26, 855-864,
641 doi:10.1007/s00382-006-0114-z, 2006.
- 642 Li, J. F., Song, Y., Mao, Y., Mao, Z. C., Wu, Y. S., Li, M. M., Huang, X., He, Q. C., and Hu,
643 M.: Chemical characteristics and source apportionment of PM_{2.5} during the harvest season in
644 eastern China's agricultural regions, *Atmos. Environ.*, 92, 442-448, 10.1016/j.atmosenv.
645 2014.04.058, 2014.
- 646 Li, M., Zhang, Q., Kurokawa, J., Woo, J., He, K., Lu, Z., Ohara, T., Song, Y., Sreets, D., and
647 Carmichael, G.: MIX: a mosaic Asian anthropogenic emission inventory for the MICS-Asia
648 and the HTAP projects, *Atmos. Phys. Chem. Discuss.*, 34813-34869, doi:10.5194/acpd-15-
649 34813-2015, 2015.
- 650 Lin, Y. L., Farley, R. D., and Orville, H. D.: Bulk Parameterization of the Snow Field in a
651 Cloud Model, *J. Clim. Appl. Meteorol.*, 22, 1065-1092, doi: 10.1175/1520-
652 0450(1983)022<1065: Bpotsf>2.0.Co;2, 1983.
- 653 Liu, Y., Fu, R., and Dickinson, R.: Smoke aerosols altering South American monsoon, *B. Am.*
654 *Meteorol. Soc.*, 86, 1062-1063, 2005.
- 655 Lo, J. C. F., Yang, Z. L., and Pielke, R. A.: Assessment of three dynamical climate
656 downscaling methods using the Weather Research and Forecasting (WRF) model, *J. Geophys.*
657 *Res. Atmos.*, 113, Artn D09112, doi:10.1029/2007jd009216, 2008.
- 658 Menon, S., Hansen, J., Nazarenko, L., and Luo, Y. F.: Climate effects of black carbon
659 aerosols in China and India, *Science*, 297, 2250-2253, doi:10.1126/science.1075159, 2002.
- 660 Mlawer, E. J., Taubman, S. J., Brown, P. D., Iacono, M. J., and Clough, S. A.: Radiative
661 transfer for inhomogeneous atmospheres: RRTM, a validated correlated-k model for the
662 longwave, *J. Geophys. Res. Atmos.*, 102, 16663-16682, doi:10.1029/97jd00237, 1997.
- 663 NBSC: China Statistical Yearbook National Bureau of Statistics of China ed., China Statistics
664 Press, Beijing, 2013.
- 665 Penner, J. E., Dickinson, R. E., and O'Neill, C. A.: Effects of Aerosol from Biomass Burning
666 on the Global Radiation Budget, *Science*, 256, 1432-1434, doi:10.1126/science.256.
667 5062.1432, 1992.
- 668 Procopio, A. S., Artaxo, P., Kaufman, Y. J., Remer, L. A., Schafer, J. S., and Holben, B. N.:
669 Multiyear analysis of amazonian biomass burning smoke radiative forcing of climate,
670 *Geophys. Res. Lett.*, 31, Artn L03108, doi:10.1029/2003gl018646, 2004.
- 671 Qian, Y., Wang, H., Zhang, R., Flanner, M.G., and Rasch, P.J.: A sensitivity study on
672 modeling black carbon in snow and its radiative forcing over the Arctic and Northern China,
673 *Environ. Res. Lett.*, 9(6), 064001, 2014.



- 674 Ramanathan, V., Chung, C., Kim, D., Bettge, T., Buja, L., Kiehl, J. T., Washington, W. M.,
675 Fu, Q., Sikka, D. R., and Wild, M.: Atmospheric brown clouds: Impacts on South Asian
676 climate and hydrological cycle, *P. Natl. Acad. Sci. USA*, 102, 5326-5333,
677 10.1073/pnas.0500656102, 2005.
- 678 Ramanathan, V., and Carmichael, G.: Global and regional climate changes due to black
679 carbon, *Nat Geosci*, 1, 221-227, 10.1038/ngeo156, 2008.
- 680 Reid, J. S., Hobbs, P. V., Liou, C., Martins, J. V., Weiss, R. E., and Eck, T. F.:
681 Comparisons of techniques for measuring shortwave absorption and black carbon content of
682 aerosols from biomass burning in Brazil, *J. Geophys. Res. Atmos.*, 103, 32031-32040, doi:10.
683 1029/98jd00773, 1998.
- 684 Reid, J. S., Koppmann, R., Eck, T. F., and Eleuterio, D. P.: A review of biomass burning
685 emissions part II: intensive physical properties of biomass burning particles, *Atmos. Chem.*
686 *Phys.*, 5, 799-825, 2005.
- 687 Robock, A.: Enhancement of Surface Cooling Due to Forest Fire Smoke, *Science*, 242, 911-
688 913, 1988.
- 689 Robock, A.: Surface Cooling Due to Forest-Fire Smoke, *J. Geophys. Res. Atmos.*, 96, 20869-
690 20878, doi:10.1029/91jd02043, 1991.
- 691 Rosenfeld, D.: TRMM observed first direct evidence of smoke from forest fires inhibiting
692 rainfall, *Geophys. Res. Lett.*, 26, 3105-3108, doi:10.1029/1999gl006066, 1999.
- 693 Rosenfeld, D., Lohmann, U., Raga, G. B., O'Dowd, C. D., Kulmala, M., Fuzzi, S., Reissell, A.,
694 and Andreae, M. O.: Flood or drought: How do aerosols affect precipitation?, *Science*, 321,
695 1309-1313, 10.1126/science.1160606, 2008.
- 696 Roy, D. P., and Boschetti, L.: Southern Africa Validation of the MODIS, L3JRC, and
697 GlobCarbon Burned-Area Products, *IEEE T. Geosci. Remote*, 47, 1032-1044,
698 10.1109/Tgrs.2008.2009000, 2009.
- 699 Ryu, S. Y., Kwon, B. G., Kim, Y. J., Kim, H. H., and Chun, K. J.: Characteristics of biomass
700 burning aerosol and its impact on regional air quality in the summer of 2003 at Gwangju,
701 Korea, *Atmos. Res.*, 84, 362-373, 10.1016/j.atmosres.2006.09.007, 2007.
- 702 Sakaeda, N., Wood, R., and Rasch, P. J.: Direct and semidirect aerosol effects of southern
703 African biomass burning aerosol, *J. Geophys. Res. Atmos.*, 116, Artn D12205, doi:
704 10.1029/2010jd015540, 2011.
- 705 Saide, P.E., Spak, S.N., Pierce, R.B., Otkin, J.A., Schaack, T.K., Heidinger, A.K., da Silva,
706 A.M., Kacenenbogen, M., Redemann, J., and Carmichael, G.R.: Central American biomass
707 burning smoke can increase tornado severity in the U.S., *Geophys. Res. Lett.*, 42, 3, 956-965,
708 2015.
- 709 Saleh, R., Robinson, E. S., Tkacik, D. S., Ahern, A. T., Liu, S., Aiken, A. C., Sullivan, R. C.,
710 Presto, A. A., Dubey, M. K., Yokelson, R. J., Donahue, N. M., and Robinson, A. L.:
711 Brownness of organics in aerosols from biomass burning linked to their black carbon content,
712 *Nat. Geosci.*, 7, 647-650, 10.1038/NGEO2220, 2014.
- 713 Schwarz, J. P., Gao, R. S., Spackman, J. R., Watts, L. A., Thomson, D. S., Fahey, D. W.,
714 Ryerson, T. B., Peischl, J., Holloway, J. S., Trainer, M., Frost, G. J., Baynard, T., Lack, D. A.,
715 de Gouw, J. A., Warneke, C., and Del Negro, L. A.: Measurement of the mixing state, mass,
716 and optical size of individual black carbon particles in urban and biomass burning emissions,
717 *Geophys. Res. Lett.*, 35, Artn L13810, doi:10.1029/2008gl033968, 2008.

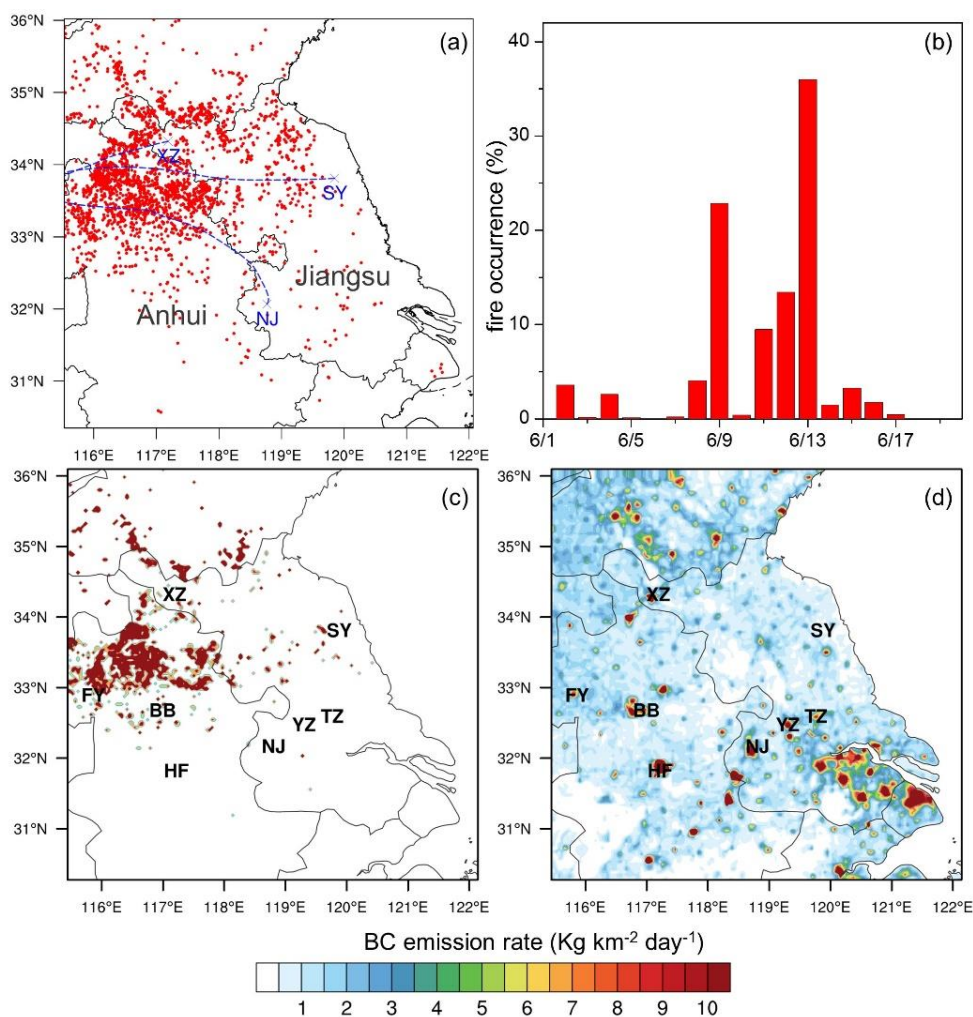


- 718 Simpson, J., Adler, R. F., and North, G. R.: A Proposed Tropical Rainfall Measuring Mission
719 (Trmm) Satellite, *B. Am. Meteorol. Soc.*, 69, 278-295, doi:10.1175/1520-0477(1988)069
720 <0278:Aptrmm>2.0.Co;2, 1988.
- 721 Tao, W. K., J. P. Chen, Z. Q. Li, C. Wang, and C. D. Zhang, Impact of Aerosols on
722 Convective Clouds and Precipitation, *Reviews of Geophysics*, 50, doi:10.1029/2011rg000369,
723 2012.
- 724 van der Werf, G. R., Randerson, J. T., Giglio, L., Collatz, G. J., Kasibhatla, P. S., and
725 Arellano, A. F.: Interannual variability in global biomass burning emissions from 1997 to
726 2004, *Atmos. Chem. Phys.*, 6, 3423-3441, 2006.
- 727 Wang, M., S. Ghan, M. Ovchinnikov, X. Liu, R. Easter, E. Kassianov, Y. Qian, and H.
728 Morrison, Aerosol indirect effects in a multi-scale aerosol-climate model PNNL-MMF,
729 *Atmos. Chem. Phys.*, 11(11), 5431-5455, doi:10.5194/Acp-11-5431-2011, 2011.
- 730 Wiedinmyer, C., Quayle, B., Geron, C., Belote, A., McKenzie, D., Zhang, X. Y., O'Neill, S.,
731 and Wynne, K. K.: Estimating emissions from fires in North America for air quality modeling,
732 *Atmos. Environ.*, 40, 3419-3432, 10.1016/j.atmosenv.2006.02.010, 2006.
- 733 Xie, Y. N., Ding, A. J., Nie, W., Mao, H. T., Qi, X. M., Huang, X., Xu, Z., Kerminen, V. M.,
734 Petaja, T., Chi, X. G., Virkkula, A., Boy, M., Xue, L. K., Guo, J., Sun, J. N., Yang, X. Q.,
735 Kulmala, M., and Fu, C. B.: Enhanced sulfate formation by nitrogen dioxide: Implications
736 from in situ observations at the SORPES station, *J. Geophys. Res. Atmos.*, 120, 12679-12694,
737 10.1002/2015JD023607, 2015.
- 738 Yan, X. Y., Ohara, T., and Akimoto, H.: Bottom-up estimate of biomass burning in mainland
739 China, *Atmos. Environ.*, 40, 5262-5273, 10.1016/j.atmosenv.2006.04.040, 2006.
- 740 Yang, S. J., He, H. P., Lu, S. L., Chen, D., and Zhu, J. X.: Quantification of crop residue
741 burning in the field and its influence on ambient air quality in Suqian, China, *Atmos. Environ.*,
742 42, 1961-1969, 10.1016/j.atmosenv.2007.12.007, 2008.
- 743 Zaveri, R. A., and Peters, L. K.: A new lumped structure photochemical mechanism for large-
744 scale applications, *J. Geophys. Res. Atmos.*, 104, 30387-30415, 1999.
- 745 Zaveri, R. A., Easter, R. C., Fast, J. D., and Peters, L. K.: Model for simulating aerosol
746 interactions and chemistry (MOSAIC), *J. Geophys. Res. Atmos.*, 113, D13204, 2008.
- 747 Zhang, Y., Fu, R., Yu, H., Qian, Y., Dickinson, R., Silva Dias, M. A. F., da Silva Dias, P. L.,
748 and Fernandes, K.: Impact of biomass burning aerosol on the monsoon circulation transition
749 over Amazonia, *Geophys. Res. Lett.*, 36, 2009.
- 750 Zhao, C., Leung, L. R., Easter, R., Hand, J., and Avise, J.: Characterization of speciated
751 aerosol direct radiative forcing over California, *J. Geophys. Res. Atmos.*, 118, 2372-2388,
752 10.1029/2012JD018364, 2013.
- 753 Zhao, T., and Yatagai, A.: Evaluation of TRMM 3B42 product using a new gauge - based
754 analysis of daily precipitation over China, *Int. J. Climatol.* 34, 2749-2762, 2014.
755



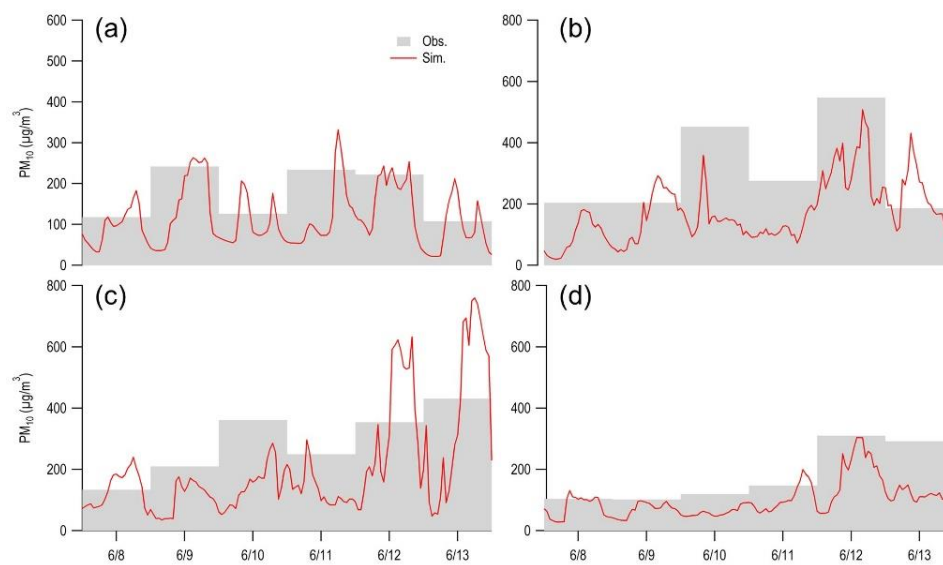
756

757 **Figure 1.** (a) Distribution of 13-year fire detections by MOD14A1 during 2003–2015 in the
758 model domain. The black rectangle represents the inner domain. The top left corner gives a
759 map showing the geographic location of the model domain. (b) 13-year time series of
760 monthly fire detections in the model domain based on MOD14A1 retrievals.



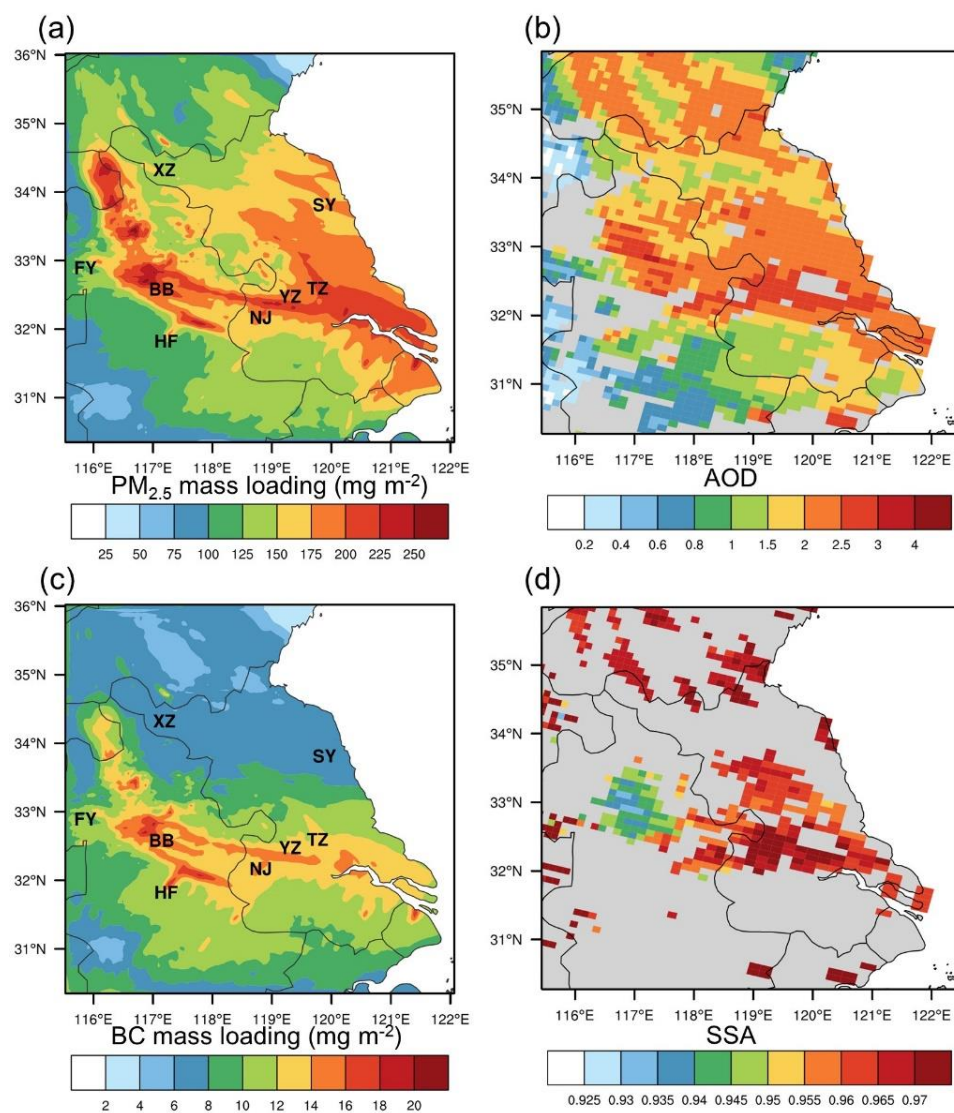
761

762 **Figure 2.** (a) Satellite fire detections in June 2012 and backward trajectories for NJ (Nanjing),
763 XZ (Xuzhou) and SY (Sheyang), (b) Temporal variations of daily fire occurrences. BC
764 emission rates from (c) agricultural fires and (d) anthropogenic activities on 9 June. Note:
765 The backward trajectories in (a) was calculated for an altitude of 2 km over NJ, XZ, and SY
766 from 14:00 LT, 18:00 LT on 10 June and 01:00 on 11 June.



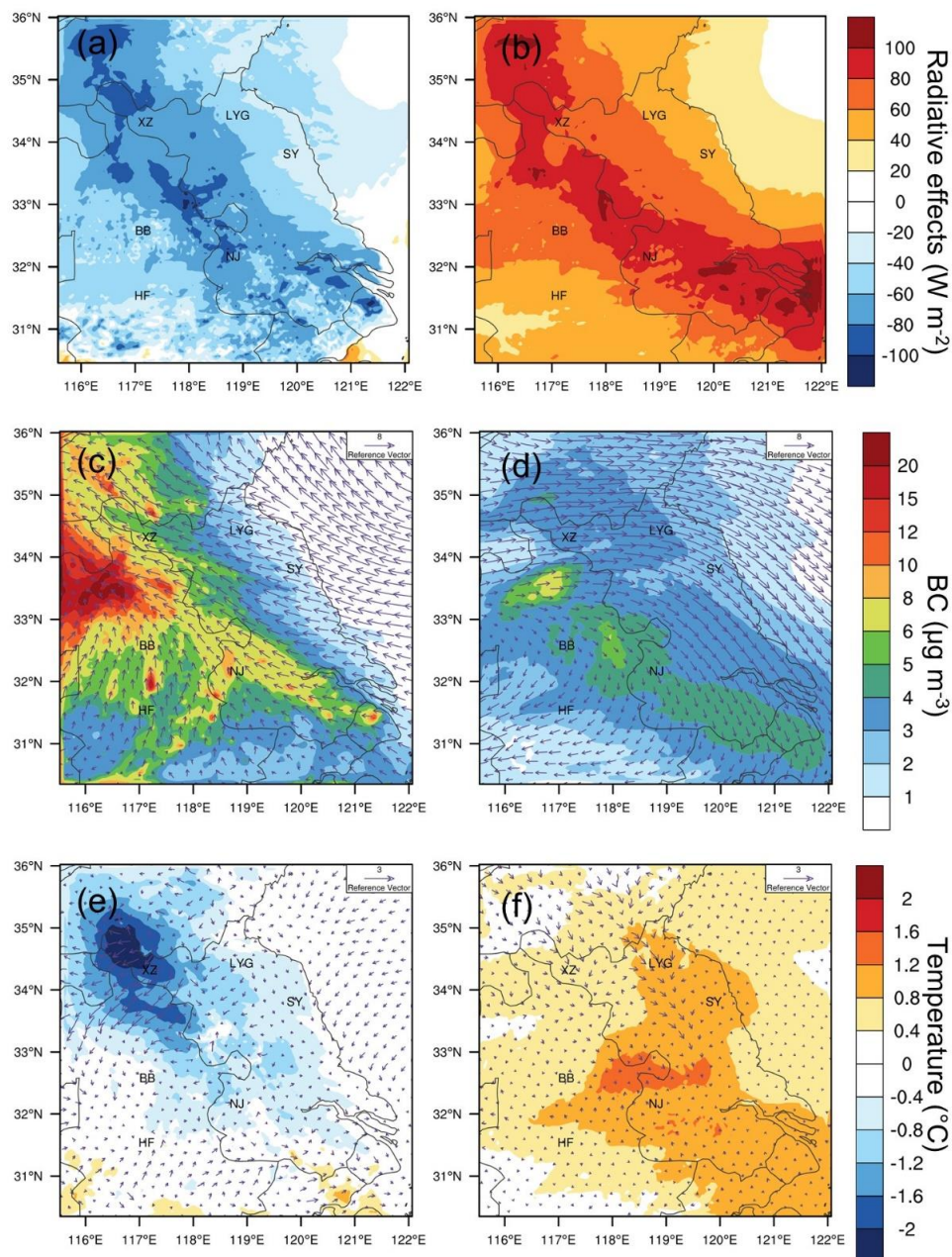
767

768 **Figure 3.** Measurements of 24-hour averaged PM10 concentrations and hourly PM10
769 simulations at (a) FY (Fuyang), (b) BB (Bengbu), (c) XZ (Xuzhou) and (d) HF (Hefei).



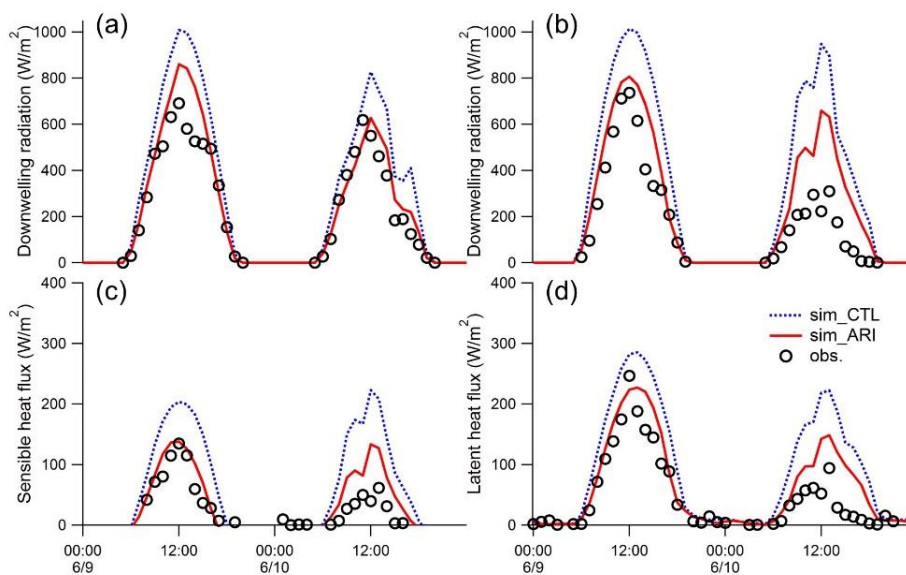
770

771 **Figure 4.** Spatial distributions of (a) simulated PM_{2.5} mass loading and (b) satellite-derived
772 660-nm AOD at 11:00 LT, 9 June. (c) simulated BC mass loading and (d) satellite-derived
773 SSA at that time.



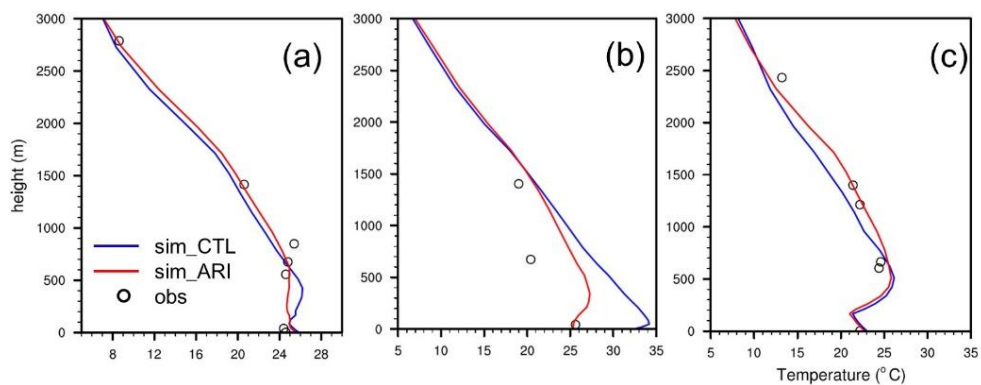
774

775 **Figure 5.** Radiative forcing of aerosol (a) at the surface and (b) in the atmosphere on 10 June.
776 Spatial pattern of daily averaged BC mass concentrations (c) near the surface and (d) at the
777 altitude of 2 km. Aerosol-induced changes in air temperature and wind fields (e) near the
778 surface and (f) at the altitude of 2 km.



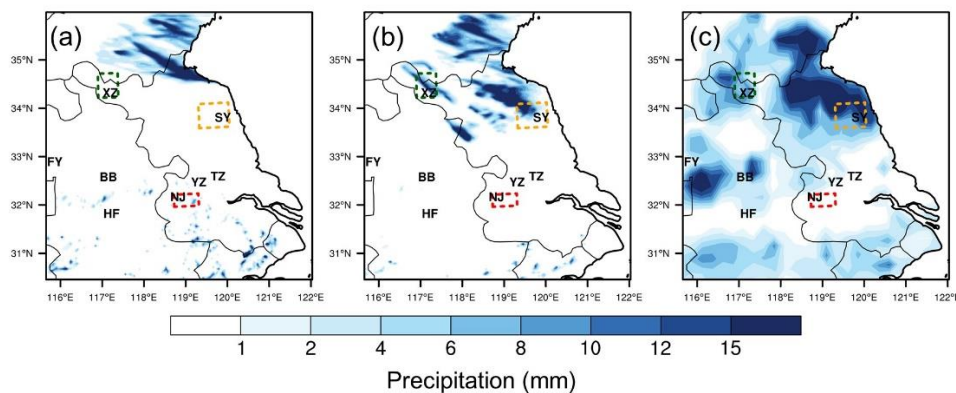
779

780 **Figure 6.** Diurnal variations of simulated and observed downwelling short-wave radiation at
781 (a) HF (Hefei) and (b) NJ (Nanjing) on 9-10, June. Comparisons of simulated sensible (c) and
782 latent heat fluxes (d) with the measurements at NJ. Blue and red lines mean CTL and ARI
783 simulation. Black circles mark the observations.



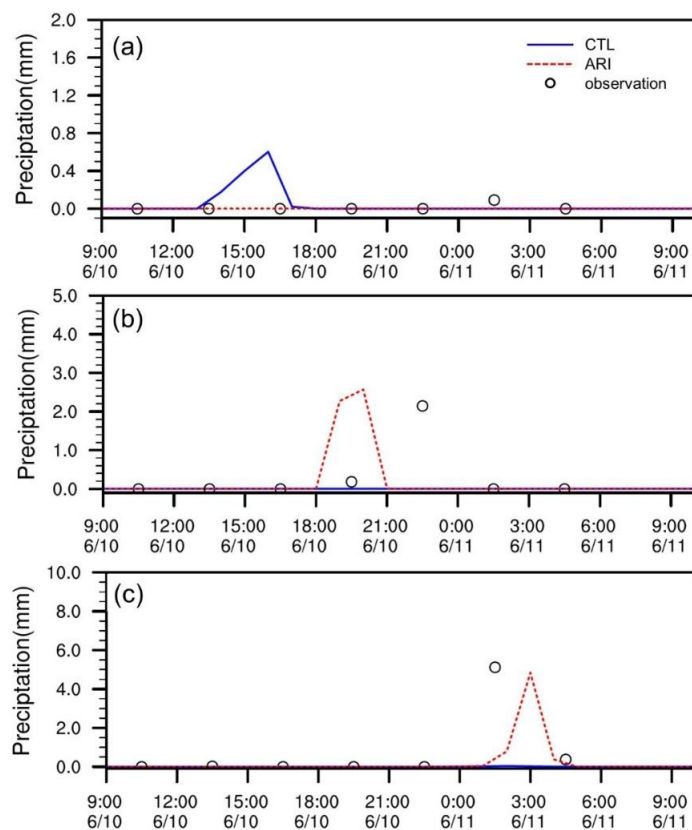
784

785 **Figure 7.** Comparisons between the observed and modelled air temperature profiles for (a) NJ
 786 (Nanjing) at 08:00LT, (b) XZ (Xuzhou) and (c) SY (Sheyang) at 20:00 LT, 10 June. Black
 787 circles denote sounding observations. Blue and red solid lines are numerical experiments
 788 without (CTL) and with radiative effects of aerosols (ARI), respectively.



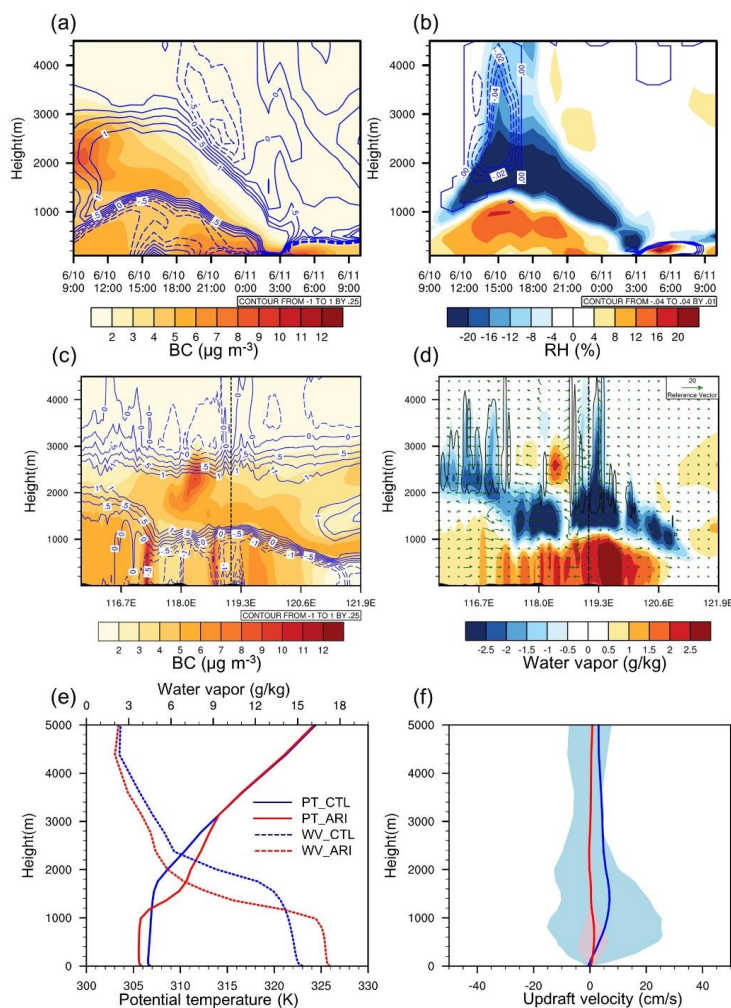
789

790 **Figure 8.** Modelled precipitation during the period from 00:00 UTC, 10 June to 00:00 UTC,
791 11 June while excluding and considering radiative effects of aerosols in CTL (a) and ARI (b)
792 experiment. (c) Corresponding TRMM-observed precipitation. Three regions with notable
793 changes in precipitation are marked in rectangles: Zone 1 (red dashed line), Zone 2 (green
794 dashed line) and Zone 3 (yellow dashed line).



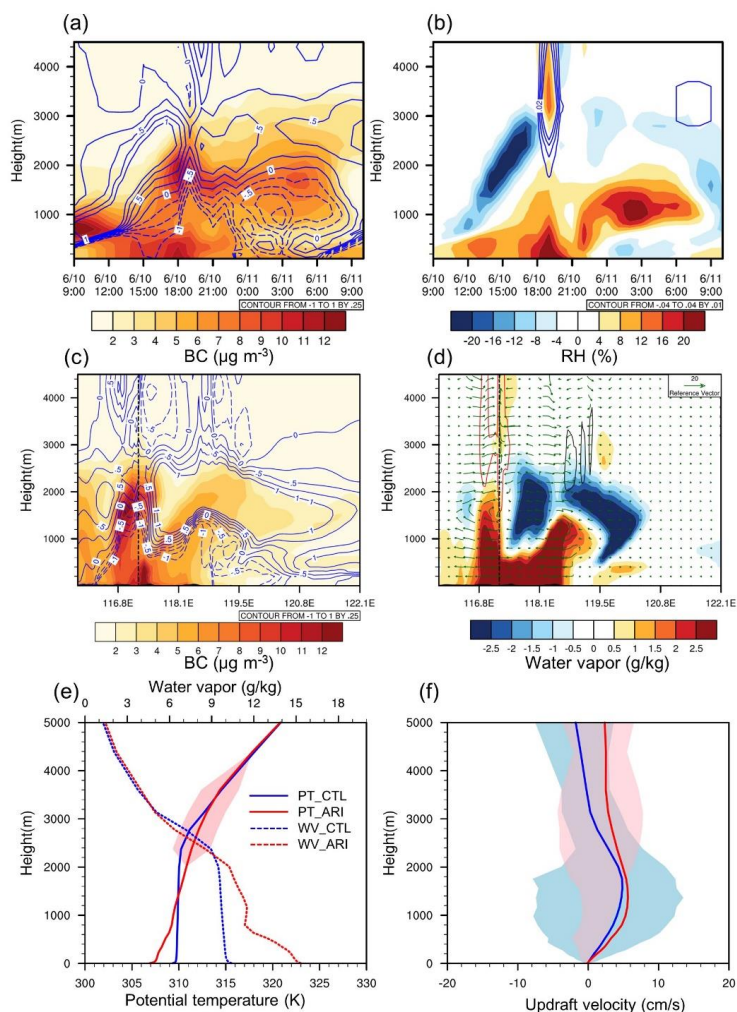
795

796 **Figure 9.** Simulated hourly precipitation while considering (red dashed lines, ARI) and
797 excluding (blue solid lines, CTL) radiative effects of aerosols, and their comparisons with
798 TRMM observations (black circles) for Zone1 (a), Zone 2 (b) and Zone 3 (c).



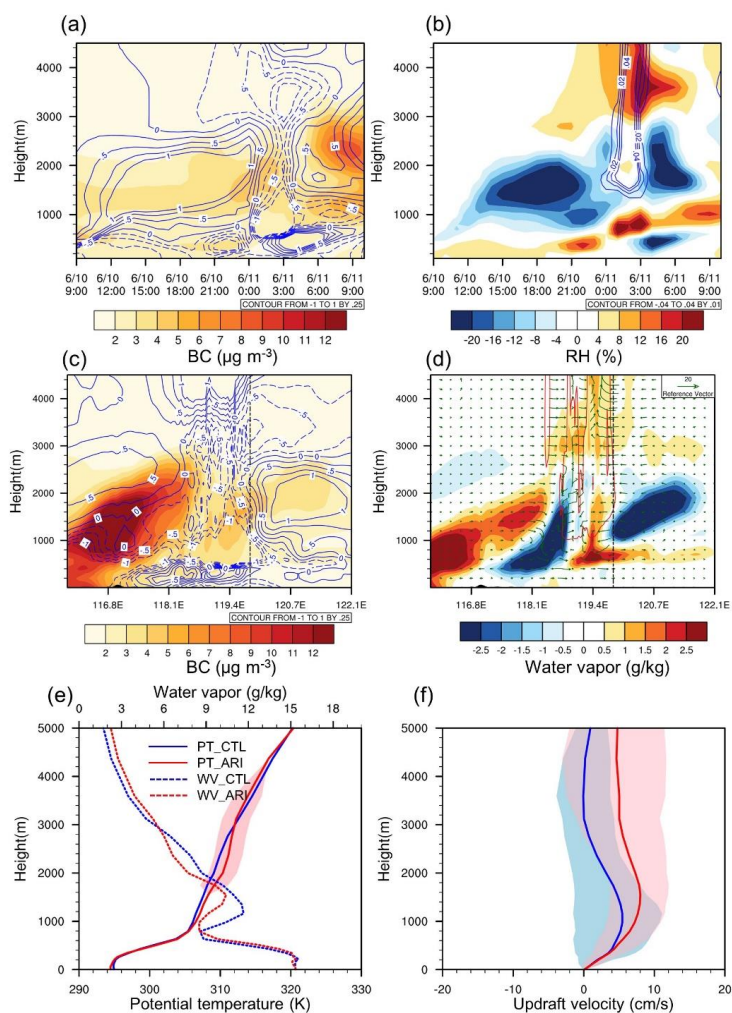
799

800 **Figure 10.** (a) Temporal evolutions of BC vertical profile and changes in air temperature (K),
 801 (b) perturbations in RH (%) and cloud water (g kg⁻¹) over Zone 1. (c) Longitude-height cross
 802 sections of BC concentrations and aerosol-induced temperature changes at 14:00 LT, 10 June.
 803 (d) same as (c) but for water vapor (g kg⁻¹) and wind fields (m s⁻¹). Note that the vertical wind
 804 speed was multiplied by a factor of 100. Red and black lines in (d) outline cloud coverage
 805 (cloud water mass ratio greater than 10⁻³ g kg⁻¹) in ARI and CTL simulation. In this case, the
 806 condensate mass ratio was less than 10⁻³ g kg⁻¹ for the whole column in ARI, thus no red line
 807 is presented in d. (e) Vertical profile of zone-averaged potential temperature (PT) and water
 808 vapor ratio (WV), and (f) updraft velocity predicted by ARI (red) and CTL (blue) at 14:00 LT.
 809 Shadows in f represent 25-75 percentile range of simulated updraft velocity.



810

811 **Figure 11.** (a) Temporal evolutions of BC vertical profile and changes in air temperature (K),
 812 (b) perturbations in RH (%) and cloud water (g kg^{-1}) over Zone 2. (c) Longitude-height cross
 813 sections of BC concentrations and aerosol-induced temperature changes at 18:00 LT, 10 June.
 814 (d) same as (c) but for water vapor (g kg^{-1}) and wind fields (m s^{-1}). Note that the vertical
 815 wind speed was multiplied by a factor of 100. Red and black lines in (d) outline cloud coverage
 816 (cloud water mass ratio greater than $10^{-3} \text{ g kg}^{-1}$) in ARI and CTL simulation. (e) Vertical
 817 profile of zone-averaged potential temperature (PT) and water vapor ratio (WV), and (f)
 818 updraft velocity predicted by ARI (red) and CTL (blue) at 18:00 LT. Shadow in e marks
 819 conditionally unstable zone in the upper air in ARI. Shadows in f represent 25-75 percentile
 820 range of simulated updraft velocity.
 821



822

823 Figure 12. (a) Temporal evolutions of BC vertical profile and changes in air temperature (K),
 824 (b) perturbations in RH (%) and cloud water (g kg⁻¹) over Zone 3. Longitude-height cross
 825 sections of BC concentrations and aerosol-induced temperature changes at 01:00 LT, 11 June
 826 (c). (d) same as (c) but for water vapor (g kg⁻¹) and wind fields (m s⁻¹). Note that the vertical
 827 wind speed was multiplied by a factor of 100. Red and black lines in (d) outline cloud
 828 coverage (cloud water mass ratio greater than 10⁻³ g kg⁻¹) in ARI and CTL simulation. In this
 829 case, the condensate mass ratio was less than 10⁻³ g kg⁻¹ for the whole column in CTL, thus no
 830 black line is presented in d. (e) Vertical profile of zone-averaged potential temperature (PT)
 831 and water vapor ratio (WV), and (f) updraft velocity predicted by ARI (red) and CTL (blue) at
 832 01:00 LT. Shadow in e marks conditionally unstable zone in the upper air in ARI. Shadows in
 833 (f) represent 25-75 percentile range of simulated updraft velocity.